Monthly Notices
of the
ROYAL ASTRONOMICAL SOCIETY

Mon. Not. R. Astron. Soc. **421,** 149–158 (2012) doi:10.1111/j.1365-2966.2011.20282.x

A *J*-band detection of the donor star in the dwarf nova OY Carinae and an optical detection of its 'iron curtain'

C. M. Copperwheat,[1⋆] T. R. Marsh,[1] S. G. Parsons,[1] R. Hickman,[1] D. Steeghs,[1] E. Breedt,[1] V. S. Dhillon,[2] S. P. Littlefair[2] and C. Savoury[2]

[1]*Department of Physics, University of Warwick, Coventry CV4 7AL*
[2]*Department of Physics and Astronomy, University of Sheffield, Sheffield S3 7RH*

Accepted 2011 November 28. Received 2011 November 25; in original form 2011 October 31

ABSTRACT

Purely photometric models can be used to determine the binary parameters of eclipsing cataclysmic variables (CVs) with a high degree of precision. However, the photometric method relies on a number of assumptions, and to date there have been very few independent checks of this method in the literature. We present time-resolved spectroscopy of the $P = 90.9$ min eclipsing CV OY Carinae obtained with X-shooter on the Very Large Telescope (VLT), in which we detect the donor star from K I lines in the *J* band. We measure the radial velocity amplitude of the donor star $K_2 = 470.0 \pm 2.7$ km s^{-1}, consistent with predictions based upon the photometric method (470 ± 7 km s^{-1}). Additionally, the spectra obtained in the *UVB* arm of X-shooter show a series of Fe I and Fe II lines with a phase and velocity consistent with an origin in the accretion disc. This is the first unambiguous detection at optical wavelengths of the 'iron curtain' of disc material which has been previously reported to veil the white dwarf in this system. The velocities of these lines do not track the white dwarf, reflecting a distortion of the outer disc that we see also in Doppler images. This is evidence for considerable radial motion in the outer disc, at up to 90 km s^{-1} towards and away from the white dwarf.

Key words: binaries: close – stars: dwarf novae – stars: individual: OY Carinae – white dwarfs.

1 INTRODUCTION

The study of close binary stars is driven by the need to understand the numbers and properties of the many possible outcomes of binary star evolution. This is of interest in many astrophysical contexts, such as the need to determine the properties of Type Ia supernova progenitors as a function of redshift, and the detection of gravitational waves, for which close binaries are predicted to be among the strongest sources (Nelemans, Yungelson & Portegies Zwart 2004). A useful population are the cataclysmic variables (CVs; Warner 1995). These close binaries consist of a white dwarf accreting matter from a main-sequence donor star, and provide us with a large, homogeneous and easily observed population which can be compared to theoretical predictions.

The binary parameters of eclipsing systems can be determined with high precision via a purely photometric method (Bailey 1979; Smak 1979; Cook & Warner 1984; Wood et al. 1986) in which the eclipse features in the light curve are used to infer the geometry of the system. The number of known eclipsing systems has increased significantly in recent years thanks to programmes such as the Sloan Digital Sky Survey (SDSS; Szkody et al. 2009), and so greater reliance has been placed on this photometric technique (see e.g. Littlefair et al. 2008; Copperwheat et al. 2010, 2011; Savoury et al. 2011b). The photometric method is based on two key assumptions: first, it is assumed that we see the bare white dwarf and can therefore measure its radius, and hence its mass, using models of white dwarf mass–radius relations. Secondly, it is assumed that the bright spot where the gas stream hits the accretion disc lies on the ballistic trajectory of the gas stream, which follows a path set by the binary mass ratio. To date there have been very few independent checks of the photometric method. Wade & Horne (1988) presented a radial velocity study of the secondary star in Z Cha, and found a value for the donor star orbital velocity $K_2 = 430 \pm 16$ km s^{-1}. In comparison, the photometric study of Wood et al. (1986) found $K_2 = 371.0 \pm 2.7$ km s^{-1}, a discrepancy of more than 3σ. This was partly attributed to an overestimation of the white dwarf radius in Wood et al. (1986), but later work accounting for this (increasing the photometric determination of K_2 to 389–406 km s^{-1}) was still $\sim 2\sigma$ different from the spectroscopic finding (Wood & Horne 1990). More recent spectroscopic studies (IP Peg, Watson et al. 2003; CTCV J1300-3052, Savoury et al. 2011a) have shown good agreement with photometric results. However, this small number of test cases is concerning, given the ubiquity of the photometric method. There have been

⋆E-mail: c.copperwheat@warwick.ac.uk

some attempts to verify the method by inferring the white dwarf orbital velocity (K_1) from the velocities of the emission lines (see e.g. Tulloch, Rodríguez-Gil & Dhillon 2009). However, these measurements are generally based on the assumption that the accretion disc is perfectly symmetric around the white dwarf. This is often not the case, and while there have been attempts to correct for a non-symmetrical disc (Marsh 1988) we would still consider these K_1 determinations to be less reliable than measurements of the donor star.

The capabilities of modern spectrographs far exceed the instrument used by Wade & Horne (1988). In particular, the wavelength range and throughput of X-shooter mounted on the European Southern Observatory (ESO) Very Large Telescope (VLT) enables us to determine a value of K_2 with a precision comparable to that which can be currently achieved via the photometric method. We therefore chose to measure this orbital velocity for the donor star in a CV and thus provide a more precise test of the light curve fitting method. The system we selected was OY Carinae (henceforth OY Car), a bright and short-period ($P = 90.9$ min) eclipsing system with a prominent white dwarf eclipse. The best photometric determinations for the binary parameters in OY Car to date were published in Littlefair et al. (2008).

2 OBSERVATIONS AND REDUCTION

We observed OY Car for a total of 1.8 h on the night of 2010 February 10 with X-shooter (D'Odorico et al. 2006) mounted on VLT UT2 (*Kueyen*). The X-shooter spectrograph consists of three independent arms (*UVB*, VIS and NIR), giving a simultaneous wavelength coverage from 3000 to 24 800 Å. We obtained 28 consecutive spectra of 185, 180 and 205 s in length for the *UVB*, VIS and NIR arms, respectively. The cycle time per exposure was ∼235 s. We binned by a factor of 2 both spatially and in the dispersion direction for the *UVB* and VIS arms, and used slit widths of 1.0, 1.2 and 0.9 arcsec for the *UVB*, VIS and NIR arms, respectively, resulting in full width at half-maximum (FWHM) spectral resolutions of 0.7, 1.0 and 2.9 Å. Weather conditions were excellent, with sub-arcsecond seeing and photometric transparency throughout.

We reduced these data using version 1.3.7 of the X-shooter pipeline. The standard recipes were used to optimally extract and wavelength calibrate each spectrum. We removed the instrumental response using observations of the spectrophotometric standard star GD 71. One complication was that, owing to an oversight, the data were obtained in 'stare' mode, rather than by nodding the object along the slit, as is typical for long-slit infrared spectroscopy. The result is that the sky subtraction is poorer than that usually possible with X-shooter. We divided our spectra by the spectrum of a telluric standard star taken at a similar airmass to reduce telluric absorption. Fortunately, most of the spectral lines we use are displaced from the worst telluric features; the optical data are not affected. We plot the averaged and continuum-subtracted spectra from all three arms in Fig. 1.

3 RESULTS

3.1 The orbital velocity of the donor star

In order to measure K_2 in Z Cha, Wade & Horne (1988) used the λλ 8183, 8194 Å Na I doublet to track the motion of the donor star. The wavelength coverage and sensitivity of X-shooter means that other absorption lines are available, and infrared spectra of M, L and T dwarfs show promising features in the *J* band (Cushing, Rayner & Vacca 2005, table 6) which have been used in previous CV studies to detect the donor star (Littlefair et al. 2000). We find the K I doublets at λλ 11 690, 11 772 Å and λλ 12 435, 12 522 Å to be much stronger features in our OY Car data compared to the Na I doublet, and we used these features to track the donor star. We plot the trailed spectra around these absorption lines in Fig. 2. Some residual telluric contamination is apparent in these trailed spectra: the 12 435 Å line is particularly affected. We masked out these sections of data when applying our model fits.

We fitted the spectra with a model consisting of a straight line and Gaussians for the *K* absorption lines, allowing the position of each Gaussian to change velocity according to

$$V = \gamma + K_2 \sin(2\pi\phi),$$

where γ is the offset of the line from its rest wavelength and ϕ is the orbital phase of the spectrum. We obtained the rest wavelengths from the National Institute of Standards and Technology (NIST) Atomic Spectra Database (Ralchenko et al. 2011). The spectra were fitted simultaneously using a Levenberg–Marquardt minimization (Press 2002), and the results are listed in Table 1. The zero-point for the orbital phase was a free parameter in these fits, and we find it to be at HJD 244 3993.548 92(4). We used the orbital period from the quadratic ephemeris given in Greenhill et al. (2006). We give the results for each line fitted individually with a single Gaussian model, as well as a combined fit in which the four lines are fitted together with a common γ, K_2 and velocity width. The combined fit gives a value of $K_2 = 470.1 \pm 2.0$ km s^{-1} for the orbital velocity of the donor star. The model fits typically give a reduced χ^2 of ∼1.4, so we rescale the uncertainties to give a reduced χ^2 of 1, and it is these values we quote in the table. We also make a second determination of the combined fit, for which we use the bootstrap method (Efron 1979; Efron & Tibshirani 1993). In this method we determine the parameter values and uncertainties via fitting a large number of individual sets of spectra which have been resampled from the original set. The two combined fits give parameter values which are in excellent agreement, with the uncertainties slightly higher for results determined via the bootstrap method. We used the combined fit as a starting point to fit each spectrum individually, and plot the resultant radial velocity curve in Fig. 3 along with the sinusoid corresponding to our orbital solution. The sinusoid is a good fit to the radial velocity – there is little to no evidence for irradiation as observed in other CVs (e.g. EX Dra, Billington, Marsh & Dhillon 1996).

The combined (bootstrap) fit gives a value of $K_2 = 470.0 \pm 2.7$ km s^{-1} for the orbital velocity of the donor star. When we fit the lines individually we find consistent values for K_2 for three of the four lines, with the 11 690 Å value around 1.5σ lower than the value for the combined fit. Our determination of the systemic velocity γ from the combined fit is 66.2 ± 2.5 km s^{-1}, although this determination is less secure since three of the individual fits result in γ values which differ significantly from the combined value. The formal errors we quote would seem to be an underestimation of the true uncertainty in this parameter at least, probably due to the telluric absorption.

Wood & Horne (1990) showed that the photometrically determined value of K_2 depends upon the white dwarf radius, the determination of which depends on the limb-darkening coefficient used. For OY Car they reported K_2 values of 470 ± 8 and 455 ± 9 km s^{-1} for a limb-darkening coefficient of $u_{\rm WD} = 0$ and 1, respectively, where the white dwarf intensity distribution is $I(\theta) = I_0(1 + u_{\rm WD} - u_{\rm WD}\cos\theta)$. However, they used a zero-temperature mass–radius relationship for the white dwarf, which introduced

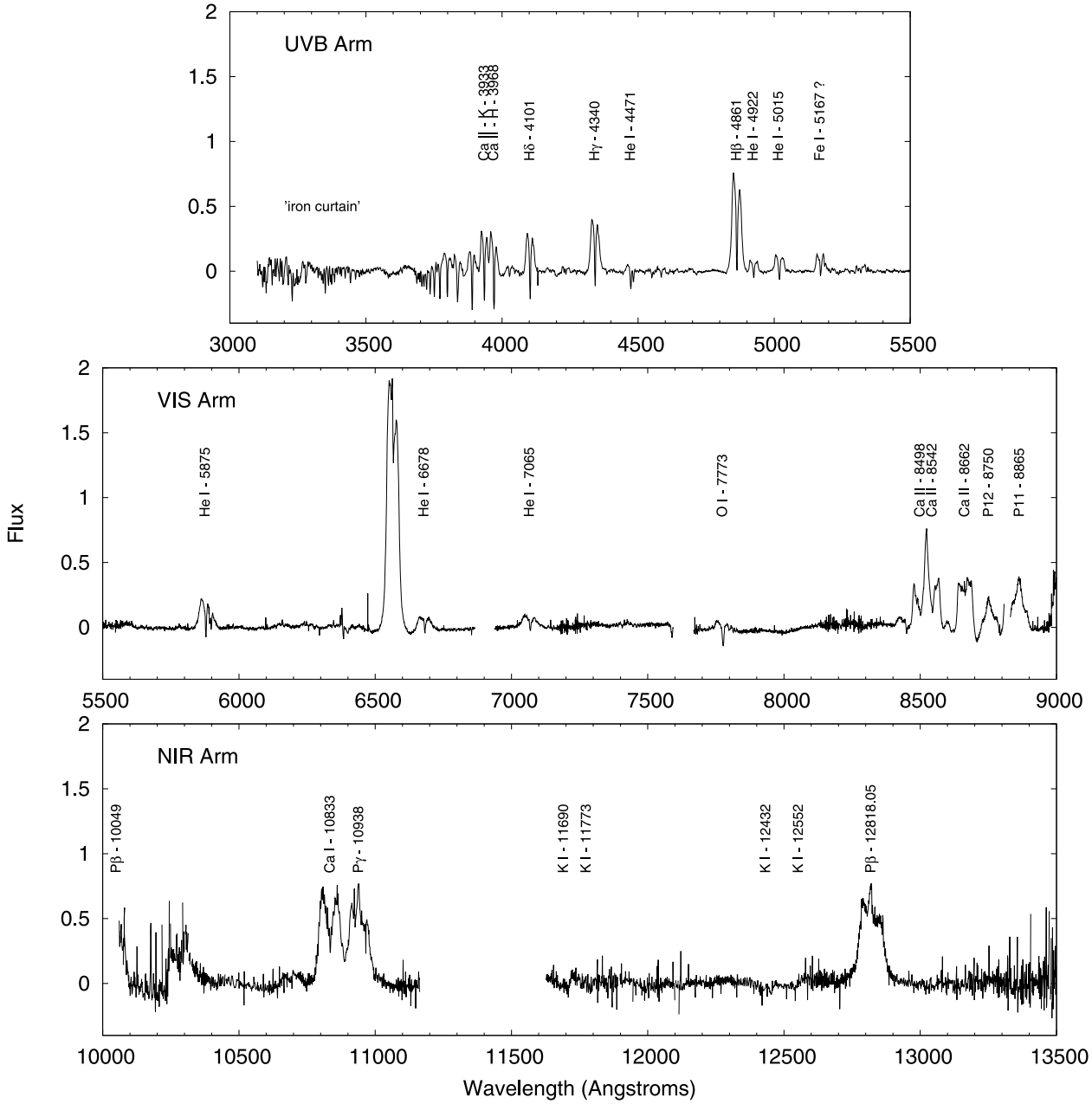

Figure 1. Averaged and continuum-subtracted spectra. The top, middle and bottom panels show the spectrum obtained in the *UVB*, VIS and NIR arms of the spectrograph, respectively. We give the wavelength in angstroms, and the panels are of different widths so as to keep the scale consistent. We identify the most prominent features, and mask out the regions of the spectrum which are most contaminated by telluric features.

a significant bias. Littlefair et al. (2008) revisited the system parameters of OY Car, and improved on the Wood & Horne (1990) determination by using a more realistic finite-temperature model for the white dwarf. They assumed $u_{\rm WD} = 0.5$ and $T_{\rm WD} = 165\,000$K (Horne et al. 1994) and find $K_2 = 470 \pm 7$ km s^{-1}. This is in excellent agreement with our spectroscopic value of 470.0 ± 2.7 km s^{-1}.

3.2 Rotational broadening of the donor star

As an additional test of the photometric parameters, we measured the rotational broadening of the donor star $V_{\rm rot}$ following the method detailed in Marsh, Robinson & Wood (1994). Using the model fit detailed in Section 3.1, we applied an offset to each spectrum to remove the orbital variation and then averaged the spectra. We then applied an artificial rotational broadening to the spectrum of a template star, and subtracted the result, multiplied by a constant representing the fraction of flux in the donor star, from the averaged OY Car spectrum. The constant was varied to optimize the subtraction, and the χ^2 difference between the residual spectrum and a smoothed version of itself is computed. This process was repeated for a range of rotational broadenings. By comparing our spectra with the spectroscopic sequence presented in Cushing et al. (2005) we identify the donor in OY Car to be a late M dwarf (M8/M9) or possibly an early T dwarf. We rule out an earlier type M dwarf since in these stars the K I features are weaker, and there are a number of Fe absorption lines of comparable strength around the λλ 11 690, 11 772 Å doublet which we do not observe in our OY Car spectra.

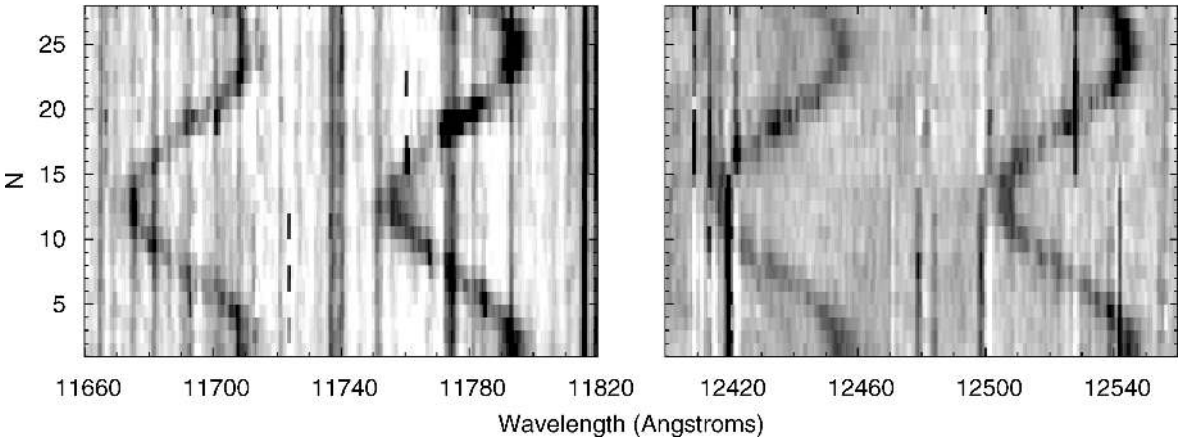

Figure 2. Trailed spectra obtained in the NIR arm. We plot the regions around the λλ 11 692, 11 778 Å and λλ 12 437, 12 528 Å K I doublets. These absorption lines move in phase with the M dwarf donor. The scale is such that the continuum is white with darker absorption features. '*N*' denotes the number of the spectrum. The $N = 19$ spectrum was obtained around phase 0.

Table 1. Parameter fits to the four K I lines observed in the NIR arm. We list the systemic velocity γ, the donor star orbital velocity K_2 and FWHM of the absorption line, which we also express in velocity units. We list the results from fitting each line individually with a single Gaussian model. The uncertainties quoted are the formal errors, scaled to give a reduced χ^2 of 1. We also list the results of combined fits obtained with a model consisting of four Gaussians. We give two combined results: one in which the uncertainties are the scaled formal errors, as for the individual fits, and a second in which we determined the parameter value and uncertainty via a bootstrap method. The bootstrap method gives slightly larger uncertainties.

Wavelength (Å)	γ (km s^{-1})	K_2 (km s^{-1})	FWHM (km s^{-1})
11 690.22	74.5 ± 4.6	457.1 ± 6.2	235.6 ± 10.8
11 772.84	58.8 ± 2.7	473.2 ± 3.4	246.6 ± 6.4
12 432.27	77.4 ± 4.3	464.1 ± 5.6	243.7 ± 8.5
12 522.14	67.4 ± 3.0	470.5 ± 4.1	206.9 ± 6.7
Combined ($\chi^2 = 1$)	66.2 ± 1.6	470.1 ± 2.0	238.9 ± 3.8
Combined (bootstrap)	66.2 ± 2.5	470.0 ± 2.7	239.1 ± 4.4

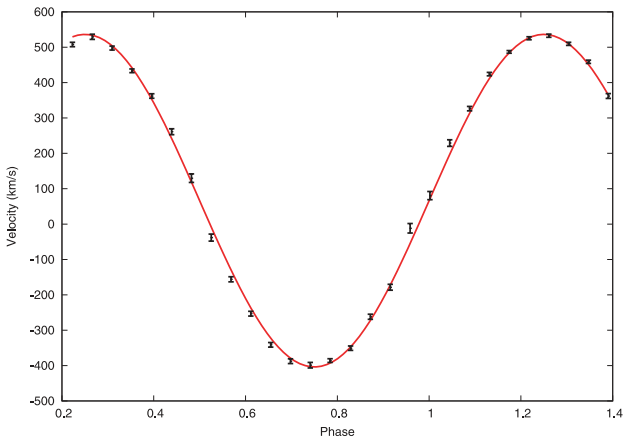

Figure 3. Radial velocity curve for the secondary star. The solid line is the sinusoid corresponding to our combined fit orbital solution, as determined in Section 3.1.

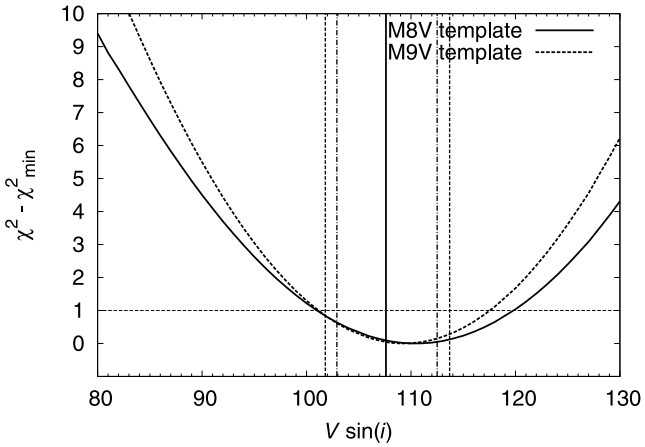

Figure 4. Curves of reduced χ^2 versus $V_{\rm rot} \sin i$, obtained via the rotational broadening measurement procedure described in Section 3.2. For the template star we use LHS 2021, an M8 dwarf (solid curve), and LHS 2065, an M9 dwarf (dashed curve). We assume a limb-darkening coefficient of 0.6. The solid vertical line marks the value of $v \sin i$ determined using the Wood & Horne (1990) binary parameters. The vertical dashed lines mark the 1σ error on this value, using the Littlefair et al. (2008) parameter uncertainties. The vertical dot–dashed lines show the uncertainty when we use our tighter constraint on K_2.

We therefore used LHS 2021 and LHS 2065 as our template stars, which are of spectral types M8 and M9, respectively. An additional input parameter is the limb-darkening coefficient for the donor star. Claret (1998) listed limb-darkening coefficients for low-mass stars, and from these tables we find that a value of $u_2 \sim 0.6$–0.7 is an appropriate J-band coefficient for the donor. We plot in Fig. 4 the resulting χ^2 curves for $u_2 = 0.6$. The minima of these curves give our preferred values of $V_{\rm rot} \sin i$, which we find to be 110 and 109 km s^{-1} for the M8 and M9 templates, respectively.

The quantity $V_{\rm rot} \sin i$ is related to the mass ratio q and K_2 via

$$V_{\rm rot} \sin i = K_2(q+1)\frac{R_2}{a}$$

(Horne, Wade & Szkody 1986), where for a Roche lobe filling star R_2/a is a function of q (Eggleton 1983). Using the photometrically determined parameters from Littlefair et al. (2008), we find $V_{\rm rot} \sin i = 108 \pm 6$ km s^{-1}. This uncertainty decreases to ± 5 km s^{-1} when we use our spectroscopically determined constraint on K_2. We

indicate this photometric determination of $V_{\rm rot}\sin i$ in Fig. 4. The figure demonstrates that, for both template stars, our spectroscopically determined value of $V_{\rm rot}\sin i$ for $u_2 = 0.6$ is consistent with the photometric value to within the uncertainties. We should note that this u_2 is appropriate for the continuum of the donor star in the *J* band, but the coefficient for the absorption lines maybe somewhat different, which would change the optimum spectroscopic value of $V_{\rm rot}\sin i$. However, we find changing u_2 in increments of 0.1 shifts the optimum value by only 1–2 km s^{-1}, and so given the uncertainty in the photometric determination of $V_{\rm rot}\sin i$, the spectroscopic value will still be consistent even if the coefficient for the lines is very different to our assumed value.

3.3 Doppler maps: emission from the disc and donor star

We create Doppler maps using a maximum entropy method (Marsh & Horne 1988; Marsh 2001) for the 4686 Å He II emission line, and the Ca II triplet at λλ 8498, 8542, 8662 Å. We plot the trailed spectra and Doppler maps in Fig. 5. The Ca II map is a single, common map to represent all three lines, with a relative scaling of 1.00, 1.25 and 1.06 for the three lines, respectively. If we examine the Ca II map first, we see a ring of emission which originates in the accretion disc. The velocity of this emission is ∼900 km s^{-1}, which is towards the high end of the range observed in other CVs (e.g. 600 km s^{-1} in U Gem; Marsh et al. 1990; see also many other examples in

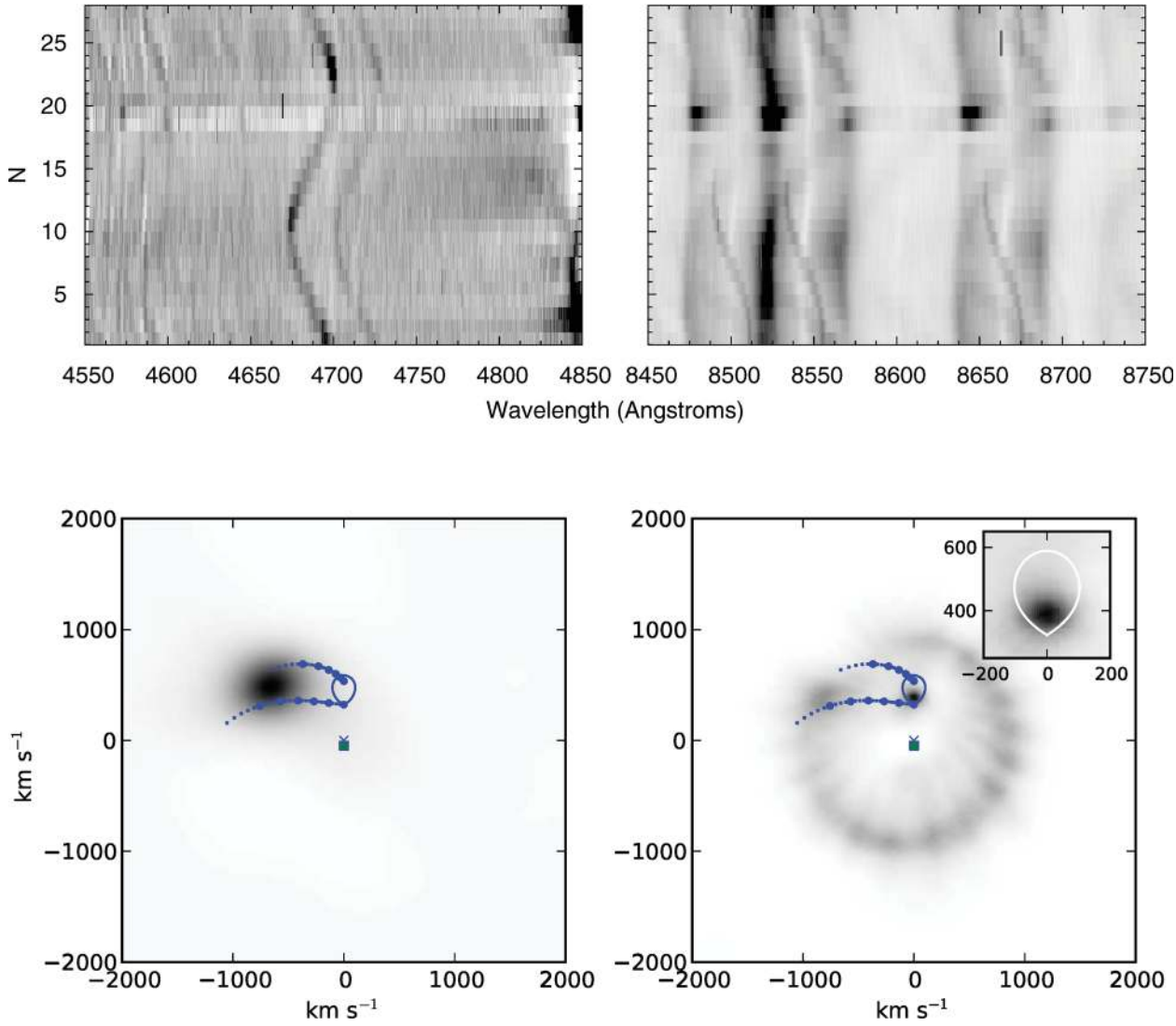

Figure 5. Top: trailed spectra around the 4686 Å He II emission line (left) and the λλ 8498, 8542, 8662 Å Ca II triplet (right). The 4713 Å He I line is also visible in the He II trail. The scale is reversed for these plots compared to the other trailed spectra in this paper, with the dark lines showing emission features rather than absorption. '*N*' denotes the number of the spectrum. The $N = 19$ spectrum was obtained around phase 0. Bottom: Doppler maps for the He II (left) and Ca II (right) emission lines. In the Ca II we produce a combined map from the three lines of the triplet. The 'spoking' evident in this map is an artefact due to the relatively low phase resolution of our spectra. We overplot in blue the Roche lobe of the donor star and the streams for a model with $q = 0.102$, $K_1 = 48$ and $K_2 = 470$ (Wood & Horne 1990). The streams denote the velocity of material in the gas stream itself (lower) and the velocity of the disc along the stream (upper). We mark the centre of mass with a cross and the position of the white dwarf with a square. Points of equal distance along the two streams are marked in units of the distance to the inner Lagrangian point from the centre of mass of the white dwarf. The small and large points mark increments of 0.02 and 0.1 of this distance, respectively.

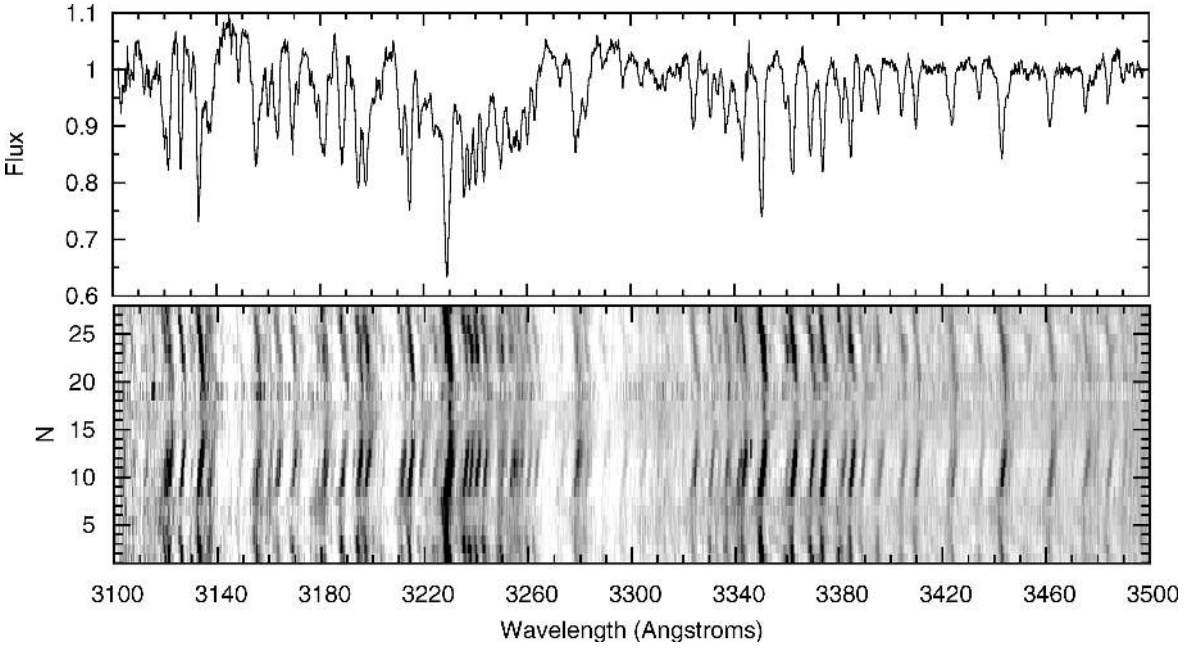

Figure 6. Bottom: trailed spectra obtained in the *UVB* arm between 3100 and 3500 Å. We observe a series of absorption lines, with a phase and velocity consistent with an accretion disc origin. The scale is such that the continuum is white with darker absorption features. '*N*' denotes the number of the spectrum. The $N = 19$ spectrum was obtained around phase 0. Top: averaged spectrum over the same wavelength range, with the velocity variations subtracted.

Kaitchuck et al. 1994). This implies a small accretion disc, and is consistent with the short orbital period and large white dwarf mass of OY Car. We also see the 'bright spot' of emission where the gas stream impacts the accretion disc, as well as Ca II emission from the donor star. This donor emission can be identified as a sharp S-wave component in the trailed spectra, and in the Doppler map we see that it is concentrated in the irradiated face of the star. We also created (but did not plot) Doppler maps of the Balmer lines. These show the same features which we observe in the Ca II map, but the donor emission is not as sharply defined.

Turning to the He II emission, in the trailed spectra we see an S-wave component with an amplitude and phase that are inconsistent with a donor star origin. In the Doppler map this emission resolves to a single component in the bright spot. Both the Ca II and He II bright spot emission have kinematics which place them between the disc and stream kinematics. The emission in both maps is quite smeared out, but the Ca II emission maybe slightly closer to the velocity of the incoming gas stream material. This would suggest that the emission in He II is from the mixture of gas stream and disc material further downstream, as is seen in other CVs (e.g. U Gem; Marsh et al. 1990).

3.4 The 'iron curtain' in the accretion disc

In the *UVB* arm (3000–5600 Å), we observe many absorption lines with a common phase and velocity. The velocity is such that these features cannot be attributed to either the white dwarf or the donor star, and so we conclude that they originate in the accretion disc. The majority of these features lie in a wavelength range of 3100–3500 Å (Fig. 6), but additional lines can be observed longwards of this to ∼5000 Å.

In Table 2, we list our identifications for these absorption lines. We find the majority to be Fe I and Fe II lines. These identifications, coupled with the evidence for an accretion disc origin, suggests that we are seeing the 'iron curtain' first identified in this system by

Table 2. Absorption features identified in the spectra obtained in the *UVB* arm. The rest wavelengths are obtained from the NIST Atomic Spectra Database (Ralchenko et al. 2011).

Line	Wavelength (Å)	Line	Wavelength (Å)
Fe I	3120.44	Fe I	3125.65
Fe I	3129.33	Fe I	3133.52
Fe I	3135.86	Fe I	3147.79
Fe II	3154.20	Fe II	3162.80
Fe I	3168.85	Fe I	3180.22
Fe II	3187.30	Fe I	3193.30
Fe I	3196.93	Fe I	3210.83
Fe II	3213.31	Fe I	3217.38
Fe I	3222.07	Fe I	3227.80
Fe I	3234.61	Fe I	3236.22
Fe II	3237.82	Fe II	3243.72
Fe I	3248.20	Fe I	3259.99
Fe I	3262.01	Fe II	3277.55
Fe II	3281.29	Fe I	3323.74
Fe I	3329.52	Fe I	3335.77
Fe I	3342.29	Fe I	3349.72
Fe II	3360.11	Fe II	3366.97
Fe I	3372.07	Fe I	3383.98
Fe II	3388.13	Fe I	3394.58
Fe I	3403.29	Fe I	3422.66
Fe I	3433.57	Fe I	3442.36
Fe I	3459.91	Ca I	3474.76
Fe I	3483.01	Fe I	3565.38
Fe I	3570.10	Fe I	3581.19
Fe I	3618.77	Fe I	3631.46
Fe I	3686.00	Fe I	3758.23
Fe I	3761.41	Fe I	4045.81
Fe II	4583.84	Fe II	4923.93
Fe II	5018.43		

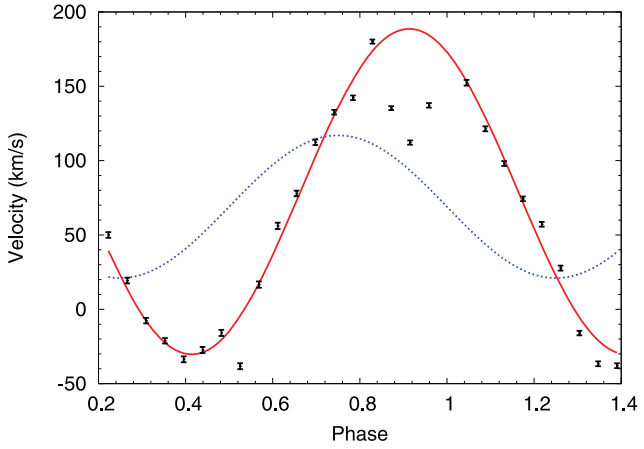

Figure 7. Radial velocity curve for the absorption lines observed in the *UVB* arm. The solid red line is the best sinusoid fit. The dashed blue line is the radial velocity curve for the white dwarf, assuming $K_1 = 48$ km s^{-1} (Wood & Horne 1990).

Horne et al. (1994). They obtained ultraviolet (UV) observations of OY Car with *Hubble Space Telescope* (*HST*) and found that the emission from the white dwarf was veiled by a forest of Fe II features, which they attributed to absorption by material from the outer accretion disc. This effect has never been directly detected before at optical wavelengths, and our optical detection is at a much higher spectral resolution than the UV *HST* data. At these longer wavelengths we find the spectra to be dominated by Fe I features, whereas Horne et al. (1994) found the majority of the absorption features in their data to be due to Fe II lines. The same effect could explain the absorption cores in the Balmer lines, which are often observed to drop below the level of the continuum in eclipsing CVs.

Using the rest wavelengths listed in Table 2, we fit each spectrum individually in the same way as we did for the donor star in Section 3.1. We plot the resulting velocities in Fig. 7. The sinusoid we plot for comparison in this figure has an amplitude of 90 km s^{-1} and a systemic velocity consistent with that derived for the donor star, and is an adequate fit to most of the velocities. There is a significant departure from this sinusoidal behaviour for the few points prior to the eclipse. This is in line with a disc origin for these absorption features since at these phases the line of sight will be through the bright spot, and so our measurements will be distorted by the complex dynamics of the disc stream interaction region. As well as the velocity, we note that the lines seem to vary in strength with phase: Fig. 6 shows them to be fainter (and also slightly broader) in the few spectra leading up to phase 0.5 ($N = 8$) and phase 0 ($N = 19$), but much stronger in the intermediate phases.

After removing the orbital velocity shifts and averaging the spectra, we fitted a subset of the iron lines and determined their FWHM to be 85.5 $\pm$ 2.9 km s^{-1}. For this subset we excluded lines which were potentially blended. We find no significant difference between the FWHM of the lines we identify as Fe I compared with those we identify as Fe II.

3.5 A simple model for the iron curtain lines

We computed a simple model which determines the absorption for a thin gas layer which rotates with the disc. This gas layer is assumed to be uniform in height, and is split into multiple sub-layers so the effect of shear can be accounted for. We use the binary parameters given in Littlefair et al. (2008) for these calculations. We considered

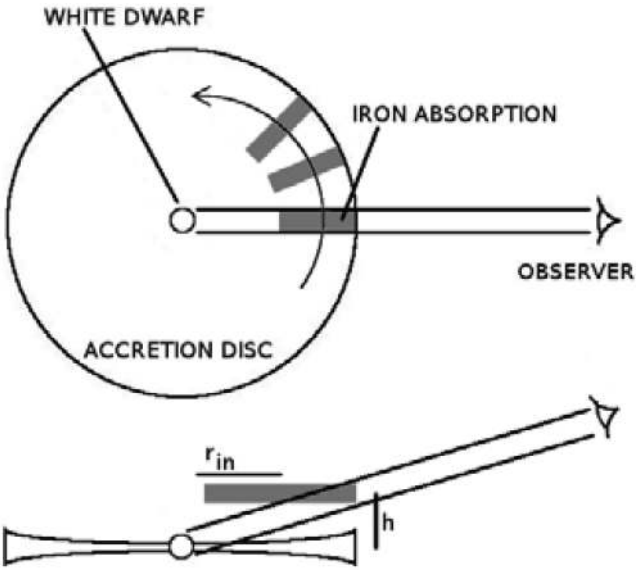

Figure 8. Cartoon showing the location of the iron absorption region. The white dwarf and the disc are not drawn to scale. The absorption region is in the outer disc and elevated at a height h above the plane of the disc, so as to lie in the line of sight between the observer and the white dwarf. The intersection of the line of sight and the gas layer is at a radial distance $r_{\rm in}$ from the white dwarf. The region of the gas layer which we observe is dependent upon the phase of the observation.

various locations for the absorbing gas layer. First, we assumed that it was very close to the white dwarf, and in the plane of the disc itself. In this configuration, the light which is absorbed originates in the lower hemisphere of the white dwarf and passes through the region of the (inclined) accretion disc which is on the line of sight to the observer. However, in this configuration our model predicts much broader absorption lines than we observe. In order for us to obtain line widths that match the observation, we require the observing region to be located in the outer accretion disc. Since the binary is inclined, this also requires the absorbing region to be elevated above the plane of the accretion disc, otherwise it would not intersect the light emitted from the white dwarf. In Fig. 8 we plot a cartoon which illustrates the small region of the disc we are probing. We define a height h above the accretion disc for the gas layer. The h we select also determines a minimum distance $r_{\rm in}$ for the *observed* region of the gas layer. Note that the gas layer is not necessarily truncated at $r_{\rm in}$, but any material closer in does not lie on the line of sight to the white dwarf and so is not observed. We do truncate the gas layer at the outer radius of the accretion disc, which we assume to be $\sim$20 white dwarf radii. Note also that as the binary phase changes the azimuth of the region we also probe changes, so if we obtain an entire orbit of time series spectra we map out an annulus of material around the disc.

In Fig. 9 we plot the region around three representative iron absorption lines in the averaged spectrum. We choose lines which are strong and relatively isolated. Some of the lines show possible emission wings as well as the absorption line: if this emission is real it presumably originates in the material which is not on the line of sight to the white dwarf. We also plot a series of model predictions. We examine first the solid lines. For all of these models we assume an rms line width of 10 km s^{-1}. We consider this an appropriate value to account for the turbulence in the disc. We plot the model in which the absorption is in the disc plane, as well as three models in which the gas layer is above the plane of the disc. We choose

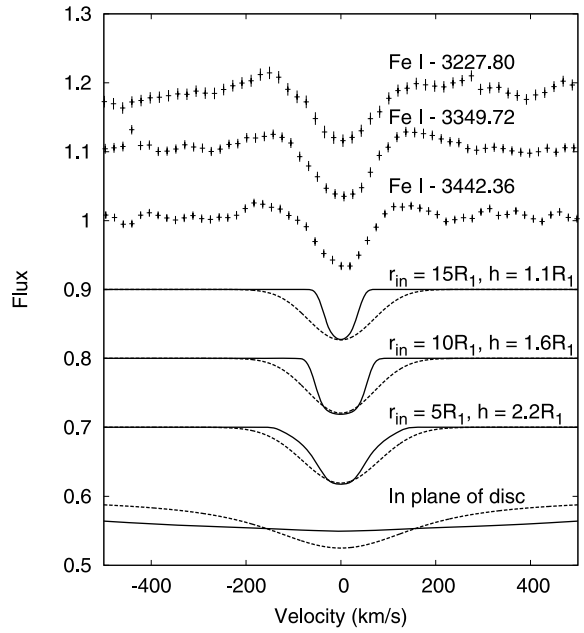

Figure 9. We show here three representative Fe lines from the iron curtain, plotting the averaged line in velocity space, with the orbital velocity variations removed. Offset below these, we show theoretical line profiles generated using the simple gas layer model described in Section 3.5. The models are offset for clarity. We express all distances in terms of the white dwarf radius R_1 (0.01 $R_\odot$; Littlefair et al. 2008). We plot three models in which the absorbing layer is above the plane of the white dwarf. We choose the height in these three layers so that the minimum radius of the *observed* region of the gas layer $r_{\rm in}$ is at a distance of 5, 10 and 15 white dwarf radii from the white dwarf itself. We also plot a model in which the gas layer is in the plane of the white dwarf, in which case all of the absorbed light originates in the lower hemisphere of the white dwarf, and the absorption occurs in the inner disc. Finally, for each model we plot two lines, one for an assumed rms line width of 10 km s^{-1} (solid), and the other for an assumed width of 60 km s^{-1} (dashed).

the heights of these three models such that $r_{\rm in}$ is 5, 10 and 15 white dwarf radii from the disc centre. We see that when the absorption region is in the plane of the disc the model line profile is much broader than is observed. If we consider the models in which the absorption region is in the outer disc, we see that as the distance of the absorbing region from the white dwarf increases the profile of the line narrows, and loses the broad wings which are observed at smaller radii. The models in which $r_{\rm in}$ is between 5 and 10 white dwarf radii are a good match to the observed line, suggesting that the iron curtain material is at a height h of 1.6–2.2 white dwarf radii above the disc plane.

Horne et al. (1994) attributed a velocity dispersion of 60 km s^{-1} to the iron curtain material they detected in the UV. In Fig. 9 the dashed lines show the same four models when we assume the rms line width to be equal to this velocity. The effect is to broaden the line profiles considerably. Many of the lines seem somewhat narrower than all of these models, and so we do not think that the velocity dispersion of the material we observe is this high. The velocity dispersion may however be somewhere between this value and our initial assumption of 10 km s^{-1}, which is a realistic minimum. This would imply a higher $r_{\rm in}$, which in turn would place the material closer in height to the plane of the disc than we determined for the 10 km s^{-1} models.

3.6 The shape of the accretion disc

As Fig. 7 shows, the radial velocities of the iron curtain do not track the velocity of the white dwarf, which we can predict with confidence given OY Car's well-determined parameters and ephemeris. The difference between the iron curtain and white dwarf velocities is evidence of significant radial motion of the material causing the absorption. For instance at phase 0, we see material receding from us at 150 km s^{-1} while the white dwarf is moving at 66 km s^{-1} away from us (the systemic velocity). This outer disc material, which is on our line of sight to the white dwarf, thus has a radial component of 84 km s^{-1} towards the white dwarf. Taking this reasoning further, if we assume that the material we see at all phases is on a single path around the white dwarf, we can integrate the radial velocity to find its radius as a function of azimuth using

$$R = R_0 + \int_0^t \frac{V_R}{\sin i}\,{\rm d}t',$$

where R_0 is an arbitrary initial radius. The $\sin i$ projection factor allows for our assumption that the motion we see is parallel to the orbital plane. We can convert this into an integral over azimuthal angle θ using $\omega = {\rm d}\theta/{\rm d}t$, whereby

$$R = R_0 + \int_0^\theta \frac{V_R}{\omega \sin i}\,{\rm d}\theta'.$$

We take ω to be given by the standard Keplerian relation for a fixed radius R_0. This ignores variations that must occur given the varying radius, but should be good to first order. We select R_0 to match the observed outer disc velocity. The azimuthal angle is directly related to the phase ϕ of Fig. 7 by $\theta = -2\pi\phi$.

To enable the integration, we fitted the velocities with four Fourier components. The result is plotted in the left-hand panel of Fig. 10. A small but significant distortion of the outer disc is evident with the main asymmetry being in the y-direction. This stands in contrast to three-body orbits such as those of Paczynski (1977) which are asymmetrical in x but not y. If the distortion deduced from the iron curtain is real, then we might expect to see it reflected in the Doppler maps, assuming that the emission lines originate from the associated gas. We therefore also predicted the equivalent path in the Doppler image shown in the right-hand side of Fig. 10 (dotted line). Due to the $v \propto R^{-1/2}$ relation between orbital speed and radius, this is even less distorted than the real-space figure, but we believe that it is in rough accord with the image, although the latter appears more distorted. We show this by plotting points marking the maximum of the emission ring. It can be seen that at most azimuths these points lie closer to the dotted, distorted path than they do to the solid, symmetrical circular path. We emphasize that the agreement here is between two independent lines of evidence: the path of the outer disc deduced from measurements of the iron curtain material as it is seen in absorption against the white dwarf versus the emission ring seen in the Ca II. The disc is shown to be non-circular, and the distortion, although small, is enough to render any measurement of K_1 from the emission lines entirely useless, as is already strongly suggested by Fig. 7. It will be interesting to establish whether hydrodynamic simulations can match our observations. We cannot tell given our single orbit whether or not the distortion we see is fixed in the rotating frame of the binary. Further epochs of observations will be needed to determine this. This distortion could, for example, be the disc ellipticity which is observed as superhumps in the light curves of SU UMa type CVs (such as OY Car) in the aftermath of superoutbursts in these systems (Hessman et al. 1992). A

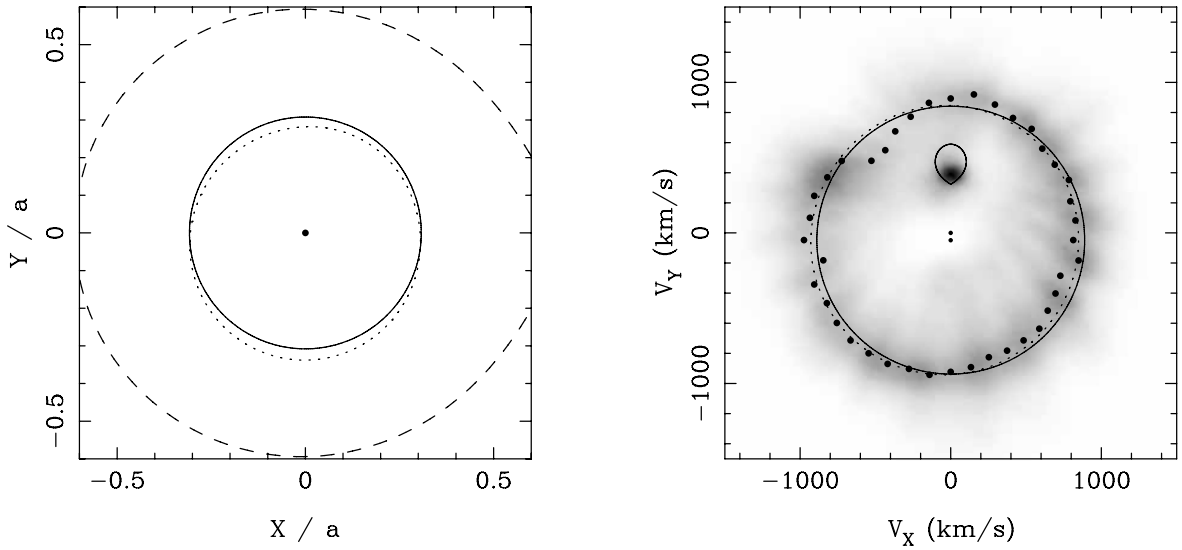

Figure 10. Left: the shape of the accretion disc, determined by fitting the iron curtain lines. The x and y coordinates are scaled by the binary separation a. When compared to a circle centred on the centre of mass (solid line), there is a distortion of the outer disc (dotted line) with the main asymmetry being in the y-direction. The dashed line shows the extent of the Roche lobe. Right: here we transform the positional information from the iron curtain fitted into velocity coordinates. Again, the dotted line shows the distortion of the outer disc as determined from the iron lines. We plot also the Ca II Doppler map, and the large dots denote the maxima of the emission ring. These maxima appear to track the iron curtain velocities more closely than the symmetrical circular path (solid). The two points in the centre of the plot show the centres of mass of the system and the white dwarf.

superoutburst was observed in OY Car from 2009 November 7 to November 21,[1] three months prior to our X-shooter observations.

4 CONCLUSIONS

In this paper we have presented high-resolution spectra of the eclipsing CV OY Car. The primary motivation of this work was to obtain a spectroscopic determination of the donor star orbital velocity to compare with the value which has been inferred from photometric models of the eclipse features ($K_2 = 470 \pm 7$ km s^{-1}). We find that two K I doublets in the J band track the motion of the donor star, and subsequently determine $K_2 = 470.0 \pm 2.7$ km s^{-1}, which is consistent with the photometric determination. As well as the absorption features from the donor star and the usual emission features seen in CVs, we also detect a forest of absorption lines concentrated in the 3100–3500 Å region. We identify the majority of these features to be Fe I and Fe II lines, and they have an approximately sinusoidal radial velocity curve with a phase and amplitude which are not consistent with a white dwarf or donor star origin. We attribute these features to the 'iron curtain' of absorbing material from the outer disc, which veils the white dwarf in this system and was first reported by Horne et al. (1994). The velocities of these lines do not track the white dwarf, reflecting a distortion of the outer disc that we see also in the Doppler images. This is evidence for considerable radial motion in the outer disc at up to 90 km s^{-1} towards and away from the white dwarf.

ACKNOWLEDGMENTS

CMC, TRM, VSD and EB are supported by rolling grants from the Science and Technology Facilities Council (STFC). DS acknowledges the support of an STFC Advanced Fellowship. The results presented in this paper are based on observations collected at ESO, Chile (Programme 084.D-1149). We also acknowledge with thanks the variable star observations from the AAVSO International Database contributed by observers worldwide and used in this research. This research has made use of NASA's Astrophysics Data System Bibliographic Services and the SIMBAD data base, operated at CDS, Strasbourg, France. We thank the reviewer Knox Long for his useful comments.

[1] Determined from data obtained by the American Association of Variable Star Observers (http://www.aavso.org/).

REFERENCES

Bailey J., 1979, MNRAS, 187, 645
Billington I., Marsh T. R., Dhillon V. S., 1996, MNRAS, 278, 673
Claret A., 1998, A&A, 335, 647
Cook M. C., Warner B., 1984, MNRAS, 207, 705
Copperwheat C. M., Marsh T. R., Dhillon V. S., Littlefair S. P., Hickman R., Gänsicke B. T., Southworth J., 2010, MNRAS, 402, 1824
Copperwheat C. M. et al., 2011, MNRAS, 410, 1113
Cushing M. C., Rayner J. T., Vacca W. D., 2005, ApJ, 623, 1115
D'Odorico S. et al., 2006, in McLean I. S., Iye M., eds, Proc. SPIE Conf. Ser. Vol. 6269, X-shooter UV- to *K*-band Intermediate-resolution High-efficiency Spectrograph for the VLT: Status Report at the Final Design Review. SPIE, Bellingham, p. 626933
Efron B., 1979, Ann. Statistics, 7, 1
Efron B., Tibshirani R. J., 1993, An Introduction to the Bootstrap. Chapman & Hall, New York
Eggleton P. P., 1983, ApJ, 268, 368
Greenhill J. G., Hill K. M., Dieters S., Fienberg K., Howlett M., Meijers A., Munro A., Senkbeil C., 2006, MNRAS, 372, 1129
Hessman F. V., Mantel K.-H., Barwig H., Schoembs R., 1992, A&A, 263, 147
Horne K., Wade R. A., Szkody P., 1986, MNRAS, 219, 791
Horne K., Marsh T. R., Cheng F. H., Hubeny I., Lanz T., 1994, ApJ, 426, 294
Kaitchuck R. H., Schlegel E. M., Honeycutt R. K., Horne K., Marsh T. R., White J. C., II, Mansperger C. S., 1994, ApJS, 93, 519
Littlefair S. P., Dhillon V. S., Howell S. B., Ciardi D. R., 2000, MNRAS, 313, 117

Littlefair S. P., Dhillon V. S., Marsh T. R., Gänsicke B. T., Southworth J., Baraffe I., Watson C. A., Copperwheat C., 2008, MNRAS, 388, 1582
Marsh T. R., 1988, MNRAS, 231, 1117
Marsh T. R., 2001, in Boffin H. M. J., Steeghs D., Cuypers J., eds, Lecture Notes in Physics, Vol. 573, Astrotomography, Indirect Imaging Methods in Observational Astronomy. Springer-Verlag, Berlin, p. 1
Marsh T. R., Horne K., 1988, MNRAS, 235, 269
Marsh T. R., Horne K., Schlegel E. M., Honeycutt R. K., Kaitchuck R. H., 1990, ApJ, 364, 637
Marsh T. R., Robinson E. L., Wood J. H., 1994, MNRAS, 266, 137
Nelemans G., Yungelson L. R., Portegies Zwart S. F., 2004, MNRAS, 349, 181
Paczynski B., 1977, ApJ, 216, 822
Press W. H., 2002, Numerical Recipes in c++: The Art of Scientific Computing. Cambridge Univ. Press, Cambridge
Ralchenko Y., Kramida A., Reader J., and NIST ASD Team 2011, NIST Atomic Spectra Database (version 4.1). National Institute of Standards and Technology, Gaithersburg, MD (available online at http://physics.nist.gov/asd)
Savoury C. D. J., Littlefair S. P., Dhillon V. S., Marsh T. R., Copperwheat C. M., Parsons S. G., 2011a, MNRAS, submitted
Savoury C. D. J. et al., 2011b, MNRAS, 415, 2025
Smak J., 1979, Acta Astron., 29, 309
Szkody P. et al., 2009, AJ, 137, 4011
Tulloch S. M., Rodríguez-Gil P., Dhillon V. S., 2009, MNRAS, 397, L82
Wade R. A., Horne K., 1988, ApJ, 324, 411
Warner B., 1995, Cambridge Astrophys. Ser. Vol. 28, Cataclysmic Variable Stars. Cambridge Univ. Press, Cambridge
Watson C. A., Dhillon V. S., Rutten R. G. M., Schwope A. D., 2003, MNRAS, 341, 129
Wood J. H., Horne K., 1990, MNRAS, 242, 606
Wood J., Horne K., Berriman G., Wade R., O'Donoghue D., Warner B., 1986, MNRAS, 219, 629

This paper has been typeset from a TEX/LATEX file prepared by the author.